Article

Where Is the Spin? Understanding Electronic Structure and g-Tensors for Ruthenium Complexes with Redox-Active Quinonoid Ligands

Christian Remenyi, and Martin Kaupp

J. Am. Chem. Soc., **2005**, 127 (32), 11399-11413• DOI: 10.1021/ja051811b • Publication Date (Web): 13 July 2005

$[Ru(acac)_2L_{NO}]^-$

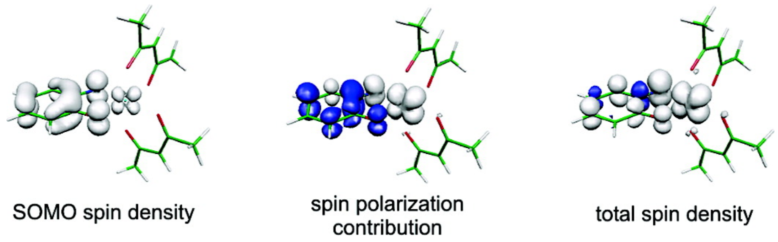

Journal of the American Chemical Society is published by the American Chemical Society. 1155 Sixteenth Street N.W., Washington, DC 20036

J|A|C|S
ARTICLES
Published on Web 07/13/2005

Where Is the Spin? Understanding Electronic Structure and g-Tensors for Ruthenium Complexes with Redox-Active Quinonoid Ligands

Christian Remenyi and Martin Kaupp*

Contribution from the Institut für Anorganische Chemie, Universität Würzburg, Am Hubland, D-97074 Würzburg, Germany

Received March 22, 2005; E-mail: kaupp@mail.uni-wuerzburg.de

Abstract: Understanding the bonding in transition metal complexes with redox-active ligands is a major challenge, for example in redox catalysis or in bioinorganic chemistry. In this work, electronic **g**-tensors, spin-density distributions, and electronic structure have been studied by different density functional methods for an extended series of complexes $[Ru(acac)_2(L)]^n$ ($n = -1, 0, +1$; L = redox-active *o*-quinonoid ligand). Comparison is made with experimental **g**-tensors and **g**-tensor-based oxidation-state assignments for a number of experimentally studied examples, using both gradient-corrected (BP86) and hybrid functionals (B3LYP, BHLYP) representing a range of exact-exchange admixtures. Reasonable, albeit not perfect, agreement with experimental **g**-tensors is obtained in one-component DFT calculations with hybrid functionals. Analyses of spin densities confirm the assignment of the cationic complexes as predominantly d^5-Ru^{III} with a neutral quinonoid ligand. However, this conclusion is obtained only after inclusion of the appreciable spin polarization of the unrestricted determinant, while the singly occupied molecular orbital (SOMO) is localized more on the acac ligands. The anionic complexes turn out to be approximately halfway between a d^6-Ru^{II}/semiquinone and a d^5-Ru^{III}/catecholate formulation, but again only after taking into account the extensive spin polarization. Even the previous assignment of the neutral parent systems as d^5-Ru^{III}/semiquinone is not accurate, as a d^6-Ru^{II}/quinone resonance structure contributes to some extent. Very unusual trends in the spin contamination of the Kohn−Sham determinant with increasing exact-exchange admixture in some of the cationic complexes have been traced to an interplay between spin delocalization and spin polarization.

1. Introduction

Redox-active ligands, sometimes termed “non-innocent” ligands, may occur in several different formal oxidation states, for example when bound to a transition metal.[1,2] Complexes with redox-active ligands are of tremendous importance in many redox processes, in particular when the transfer of more than one electron is required, for example in certain metalloenzymes.[3] Prime examples in nature are tetrapyrrol-based ligands (e.g., porphyrins), pterins, flavins, quinones, dithiolenes, or phenoxyl-based systems. The possible change of ligand oxidation state makes it difficult to assign unambiguous “physical”[4] oxidation numbers to the metal center. In open-shell cases, EPR spectroscopy has often been used to estimate the spin distribution from experimental data, and to subsequently assign oxidation numbers. Quantum chemical calculations provide independent access to EPR parameters, and to density and spin-density distributions. As spin delocalization and spin polarization mechanisms tend to be pronounced in transition metal systems, the use of quantum-chemical methods has proven to provide particularly valuable insights into electronic structure,[5−7] and thus indirectly into physical oxidation states, provided that a clear-cut assignment of charge and/or spin to metal and ligands is possible.

Here we use density functional theory (DFT) to evaluate **g**-tensors and spin density distributions of a series of anionic and cationic ruthenium complexes with *o*-quinonoid ligands. DFT is well suited for spin-density analyses of transition metal complexes of appreciable size, as has been shown recently, for example by comparison to post-Hartree−Fock spin densities for iron porphyrin complexes.[8] The particular systems we have chosen here are based on a recent experimental study by Patra et al.[9] Using X-ray and EPR methods, they investigated complexes $[Ru(acac)_2L]^{+1/0/-1}$, where L is an *o*-iminoquinone or *o*-iminothioquinone (Figure 1 provides examples for the two

---

(1) Jörgensen, C. K. *Oxidation Numbers and Oxidation States*; Springer: Heidelberg, Germany, 1969.
(2) Ward, M. D.; McCleverty, J. A. *J. Chem. Soc., Dalton Trans.* **2002**, 275.
(3) See, e.g., Kaim, W.; Schwederski, B. *Pure Appl. Chem.* **2004**, *76*, 351 and references therein.
(4) For a discussion on the distinction between formal and physical oxidation numbers in complexes with “non-innocent” ligands, see: Chaudhuri, P.; Verani, C. N.; Bill, E.; Bothe, E.; Weyhermüller, T.; Wieghardt, K. *J. Am. Chem. Soc.* **2001**, *123*, 2213 and references therein.
(5) Cano, J.; Ruiz, E.; Alvarez, S.; Verdaguer, M. *Comments Inorg. Chem.* **1998**, *20*, 27.
(6) Johansson, M. P.; Sundholm, D.; Gerfen, G.; Wikström, M. *J. Am. Chem. Soc.* **2002**, *124*, 11771.
(7) Ray, K.; Begum, A.; Weyhermueller, T.; Piligkos, S.; Van Slageren, J.; Neese, F.; Wieghardt, K. *J. Am. Chem. Soc.* **2005**, *127*, 4403.
(8) Johansson, M. P.; Sundholm, D. *J. Chem. Phys.* **2004**, *120*, 3229.
(9) Patra, S.; Sarkar, B.; Mobin, S. M.; Kaim, W.; Lahiri, G. K. *Inorg. Chem.* **2003**, *42*, 6469.

10.1021/ja051811b CCC: $30.25

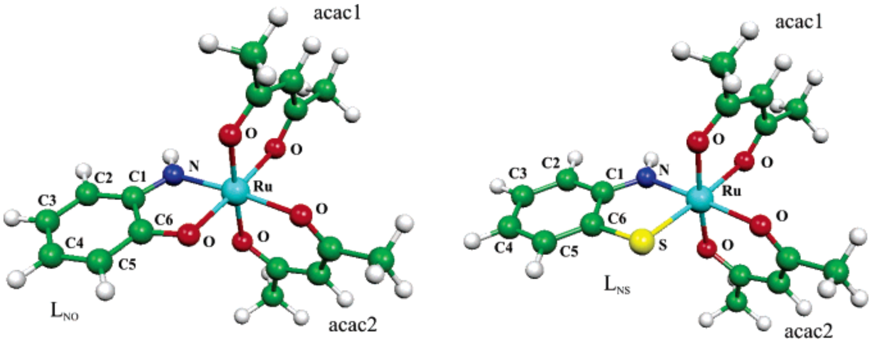

Figure 1. Structures, atom and ligand labels for (a) $[Ru(acac)_2(L_{NO})]^+$ and (b) $[Ru(acac)_2(L_{NS})]^-$.

Scheme 1. Alternative Formulations for the Oxidized and Reduced States of $[Ru(acac)_2(L)]$ (scheme taken from ref 9)

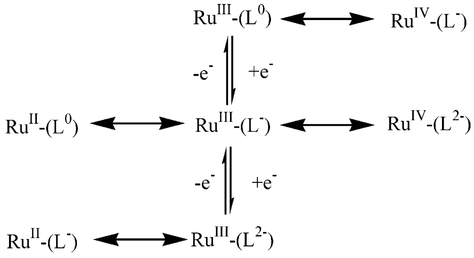

experimentally studied cases). *o*-Quinone-type ligands have received particular attention from synthetic, structural, and spectroscopic studies, due to their unique ability to stabilize transition metals in unusual electronic situations[10,11] (this includes catecholate and dithiolene complexes). Examples for biological *o*-quinone-type ligands include pyrroloquinolinequinone (PQQ) or topaquinone (TPQ), often coupled to copper.[12−14] Other related biological systems are catecholate complexes with iron, for example in the iron transfer protein enterobactin or other siderophores.[15] In some cases, even thermally activated redox tautomerism has been found.[14]

In principle, the *o*-quinonoid ligands L may exist in three oxidation states, neutral quinone (L), anionic semiquinone (L^-), and dianionic catecholate (L^{2-}). The most likely oxidation state assignments to the metal in the neutral, monoanionic, and monocationic ruthenium title complexes are shown in Scheme 1. The X-ray structure of the neutral *o*-iminoquinone complex $[Ru(acac)_2[(L_{NO})]$ was interpreted to suggest a +III metal oxidation state and a semiquinone anionic ligand. In agreement with this assignment, the neutral complex is in an EPR-silent singlet ground state. The assignments for the oxidized and reduced forms for these and related ruthenium complexes with *o*-quinonoid ligands were mainly based on **g**-tensor anisotropies and deviations of the isotropic *g*-value from the free-electron value.[9,16,17] It was concluded that in both charged states of the complexes with anionic acac coligands, a formulation with an oxidation-state Ru^{III} is most appropriate.[9] This would require a neutral quinone for the cationic system and the catecholate state for the anionic complex. The two-electron oxidation/reduction processes that link cationic and anionic complexes would thus be purely ligand-centered. In most related cases of ruthenium systems with neutral diimine-type coligands, a formulation with Ru^{II} was preferred,[18] whereas the corresponding osmium complexes were closer to Os^{III}.[19] Very recently, these assignments were questioned, based on the structural data available and based on an independent study of nickel and cobalt complexes with *o*-iminoquinone and *o*-diiminoquinone ligands.[20]

The **g**-tensor is the property that probably provides the most compact experimental image of the spin-density distribution in a molecule. Simple models relating **g**-tensor data to spin-density distribution and thus to electronic structure exist for "normal" transition metal complexes with metal-centered spin density as well as for organic π-radicals. While ligand-field theory is typically used for interpretation in the former case (see, e.g., refs 21−23), Stone's MO model[24] allows a good qualitative understanding for the latter. However, no similarly intuitive rules exist as yet for transition metal complexes, when the spin is significantly delocalized between metal and ligands.[25] It is clear that a large spin−orbit (SO) coupling constant of the metal compared to small SO coupling with only light ligand atoms should lead to larger **g**-tensor anisotropy with increased spin density on the metal. However, this knowledge alone does not allow detailed insights into the electronic structure of the complex to be derived from the measured **g**-tensor. It is thus important to come to a deeper understanding of the interrelations between **g**-tensor and spin-density distribution for such systems. This may be achieved best by quantum chemical calculations on suitable model complexes. Due to the size of the systems of interest, DFT provides the most suitable methodological basis.[26−33]

---

(10) Lubitz, W.; Lendzian, F.; Bittl, R. *Acc. Chem. Res.* **2002**, *35*, 313.

(11) (a) Pierpont, C. G. *Coord. Chem. Rev.* **2001**, *216*, 99. (b) Pierpont, C. G. *Coord. Chem. Rev.* **2001**, *219*, 415.

(12) Duine, J. A. *J. Biosci. Bioeng.* **1998**, *88*, 231.

(13) (a) Land, E. J.; Ramsden, C. A.; Riley, P. A. *Acc. Chem. Res.* **2003**, *36*, 300. (b) Que, L., Jr. In *Bioinorganic Catalysis*; Reedijk, J., Ed.; Marcel Dekker: New York, 1993; p 347.

(14) Rall, J.; Wanner, M.; Albrecht, M.; Hornung, F. M.; Kaim, W. *Chem. Eur. J.* **1999**, *5*, 2802.

(15) See, e.g.: Karpishin, T. B.; Gebhard, M. S.; Solomon, E. I.; Raymond, K. N. *J. Am. Chem. Soc.* **1991**, *113*, 297 and references therein.

(16) Kaim, W. *Coord. Chem. Rev.* **1987**, *76*, 187.

(17) (a) Ernst, S. D.; Kaim, W. *Inorg. Chem.* **1989**, *28*, 1520. (b) Ernst, S.; Haenel, P.; Jordanov, J.; Kaim, W.; Kasack, V.; Roth, E. *J. Am. Chem. Soc.* **1989**, *111*, 1733.

(18) See, e.g.: (a) Masui, H.; Lever, A. B. P.; Auburn, P. A. *Inorg. Chem.* **1991**, *30*, 2402. (b) Das, C.; Kamar, K. K.; Ghosh, A. K.; Majumdar, P.; Hung, C.-H.; Goswami, S. *New J. Chem.* **2002**, *26*, 1409.

(19) Haga, M.-A.; Isobe, K.; Boone, S. R.; Pierpont, C. G. *Inorg. Chem.* **1990**, *29*, 3795.

(20) Bill, E.; Bothe, E.; Chaudhuri, P.; Chlopek, K.; Herebian, D.; Kokatam, S.; Ray, K.; Weyhermüller, T.; Neese, F.; Wieghardt, K. *Chem. Eur. J.* **2005**, *11*, 204.

(21) Abragam, A.; Pryce, M. H. L. *Proc. R. Soc. London, Ser. A* **1951**, *205*, 135.

(22) Abragam, A.; Bleaney, B. *Electron Paramagnetic Resonance of Transition Ions*; Clarendon Press: Oxford, 1970.

(23) McGarvey, B. R. In *Transition Metal Chemistry: A Series of Advances*; Carlin, R. L., Ed.; New York, 1966; Vol. 3, pp 89−201.

(24) (a) Stone, A. J. *Proc. R. Soc. (London)* **1963**, *A271*, 424. (b) Stone, A. J. *Mol. Phys.* **1963**, *6*, 509. (c) Stone, A. J. *Mol. Phys.* **1964**, *7*, 311.

(25) Frantz, S.; Hartmann, H.; Doslik, N.; Wanner, M.; Kaim, W.; Kuemmerer, H.-J.; Denninger, G.; Barra, A.-L.; Duboc-Toia, C.; Fiedler, J.; Ciofini, I.; Urban, C.; Kaupp, M. *J. Am. Chem. Soc.* **2002**, *124*, 10563.

(26) Schreckenbach, G.; Ziegler, T. *J. Phys. Chem. A* **1997**, *101*, 3388.

(27) Patchkovskii, S.; Ziegler, T. *J. Chem. Phys.* **1999**, *111*, 5730.

As the spin-density distribution and the computed **g**-tensors of transition metal complexes have been found to depend sensitively on the exchange-correlation functional used in such DFT calculations, we use in the present work three different functionals with variable Hartree−Fock exchange admixture to study **g**-tensor and spin-density distribution. This is done for the experimentally investigated systems of Patra et al.[9] with *o*-iminoquinone, L_{NO}, and *o*-iminothioquinone, L_{NS} (we provide also a study of the two neutral complexes), as well as for the as yet not studied analogues with symmetrical *o*-quinone (L_{OO}; related to benzenediolato), *o*-diiminoquinone (L_{NN}; related to *o*-phenylenediamine), and *o*-dithioquinone (L_{SS}; related to benzenedithiolato) ligands.

As the combination of analysis methods employed provides an unprecedentedly detailed picture of charge and spin-density distributions for the different charge states of the title complexes, rather general conclusions may be drawn on the interrelations between structure, spectroscopy, and electronic structure of complexes with *o*-quinonoid ligands.

2. Methods

Formalism of g-Tensor Calculations. The theoretical background of EPR parameters is covered in detail in text books;[22,23,34−36] hence, we summarize only the most relevant points. We will provide both absolute *g*-values and *g*-shifts, $\Delta\mathbf{g}$, which represent the deviation from the free electron value (given here in ppt, i.e., in units of 10^{-3}),

$$\mathbf{g} = g_e\mathbf{1} + \Delta\mathbf{g} \tag{1}$$

with $g_e = 2.002319$. We use second-order perturbation theory, initially based on the Breit−Pauli Hamiltonian. Hence, the *g*-shift consists of three terms,

$$\Delta\mathbf{g} = \Delta\mathbf{g}^{\mathrm{SO/OZ}} + \Delta\mathbf{g}^{\mathrm{RMC}} + \Delta\mathbf{g}^{\mathrm{GC}} \tag{2}$$

of which the "paramagnetic" second-order spin−orbit/orbital Zeeman cross term, $\Delta\mathbf{g}^{\mathrm{SO/OZ}}$, dominates (except for extremely small $\Delta\mathbf{g}$ values).[34] Within our coupled-perturbed Kohn−Sham (CPKS) implementation, using (nonlocally implemented) hybrid density functionals, and based on unrestricted Kohn−Sham wave functions, its Cartesian components *u*,*v* are computed as[32]

$$\Delta\mathbf{g}_{uv}^{\mathrm{SO/OZ}} = \frac{\alpha^2}{2}g_e\left[\sum_k^{\mathrm{occ}(\alpha)}\sum_a^{\mathrm{virt}(\alpha)}\frac{\langle\psi_k^\alpha|h_v^{\mathrm{SO}}|\psi_a^\alpha\rangle\langle\psi_a^\alpha|F'_{k,v}|\psi_k^\alpha\rangle}{\epsilon_k^\alpha-\epsilon_a^\alpha} - \sum_k^{occ(\beta)}\sum_a^{virt(\beta)}\frac{\langle\psi_k^\beta|h_v^{\mathrm{SO}}|\psi_a^\beta\rangle\langle\psi_a^\beta|F'_{k,v}\psi_k^\beta\rangle}{\epsilon_k^\beta-\epsilon_a^\beta}\right] \tag{3}$$

where α is the fine-structure constant and h_{SO} is the one- and two-electron spin−orbit (SO) Hamiltonian. F'_K is the perturbed Fock operator, with $F'_K = l_{\mathrm{O}} - (2/\alpha)a_0 \sum_{k=1}^{n/2}F'_{k,v}$, where l_{O} is a spatial component of the orbital Zeeman operator, $F'_{k,v}$ is the response exchange operator, and a_0 is the weight of HF exchange, depending on the specific hybrid functional used. ψ^σ and ϵ^σ are spin-polarized Kohn−Sham orbitals and orbital energies, respectively. GGA or LDA functionals lead to an uncoupled DFT (UDFT) treatment for this second-order term ($a_0 = 0$). The relativistic mass correction term Δg^{RMC} and the one-electron part of the gauge correction term Δg^{GC} are also included in our approach[28,32] (see also refs 26 and 31 for related implementations).

Computational Details. All structure optimizations employed the Turbomole 5.6 program,[37] at unrestricted Kohn−Sham (UKS) level. A quasi-relativistic small-core pseudopotential (effective-core-potential, ECP)[38] and a [7s6p5d]/(5s3p2d) valence basis set[39] were used for Ru, together with DZVP all-electron basis sets[40] for C, N, O, S, and H. Exchange-correlation functionals to be compared are the BP86 generalized gradient approximation (GGA),[41,42] as well as the hybrid B3LYP[43,44] and BHLYP[45,46] functionals. This sequence corresponds to 0%, ca. 20%, and 50% Hartree−Fock exchange admixture, respectively. For the BP86 GGA functional, the Coulombic term was evaluated by density fitting (RI-DFT method), with SVP auxiliary basis sets.[47]

Calculation of the **g**-tensor was done in each case using the structure and Kohn−Sham wave function for a given functional, as obtained from the structure optimizations above. The unrestricted Kohn−Sham orbitals were transferred by suitable interface routines to the in-house MAG-ReSpect property package,[48] which was used for the **g**-tensor calculations. A common gauge origin at the metal nucleus was employed. The SO operator h_{SO} in eq 3 was made up from an accurate and efficient[28,32] superposition of a spin−orbit pseudopotential (SO-ECP) on Ru[38] and all-electron Breit−Pauli atomic mean-field (AMFI)[49,50] SO operators for the ligand atoms.

Natural atomic charges[51] from natural population analyses (NPA) were obtained with a stand-alone version of the NBO4.M program,[52] interfaced to Turbomole in our group.[53] NPA and Mulliken[54] spin densities were found to be very similar. We will refer to Mulliken spin densities, as it was easier to access them for individual MOs. Molecular structures, canonical and natural orbitals, and spin-density isosurfaces are displayed with the Molekel 4.3 program.[55] To analyze canonical MOs in strongly spin-polarized Kohn−Sham wave functions, we have employed overlap criteria to identify the corresponding spin-up and

---

(28) Malkina, O. L.; Vaara, J.; Schimmelpfennig, B.; Munzarová, M.; Malkin, V. G.; Kaupp, M. *J. Am. Chem. Soc.* **2000**, *122*, 9206.
(29) Patchkovskii, S.; Ziegler, T. *J. Am. Chem. Soc.* **2000**, *122*, 3506.
(30) van Lenthe, E.; van der Avoird, A.; Hagen, W. R.; Reijerse, E. J. *J. Phys. Chem. A* **2000**, *104*, 2070.
(31) Neese, F. *J. Chem. Phys.* **2001**, *115*, 11080.
(32) Kaupp, M.; Reviakine, R.; Malkina, O. L.; Arbuznikov, A.; Schimmelpfennig, B.; Malkin, V. G. *J. Comput. Chem.* **2002**, *23*, 794.
(33) Kaupp, M., Bühl, M., Malkin, V. G., Eds. *Calculation of NMR and EPR Parameters: Theory and Applications*; Wiley-VCH: Weinheim, 2004.
(34) Harriman, J. E. *Theoretical Foundations of Electron Spin Resonance*; Academic Press: New York, 1978.
(35) Atherton, N. M. *Principles of Electron Spin Resonance*; Prentice Hall: New York, 1993.
(36) Mabbs, F. E.; Collison, D. *Electron Paramagnetic Resonance of d Transition Metal Compounds*; Elsevier: Amsterdam, 1992.
(37) Ahlrichs, R.; Bär, M.; Häser, M.; Horn, H.; Kölmel, C. *Chem. Phys. Lett.* **1989**, *162*, 165. See also: Ahlrichs, R.; von Arnim, M. In *Methods and Techniques in Computational Chemistry: METECC-95*; Clementi, E., Corongiu, G., Eds.; Club Européen MOTECC: Belgium, 1995; Chapter 13, pp 509 ff.
(38) Andrae, D.; Häussermann, U.; Dolg, M.; Stoll, H.; Preuss, H. *Theor. Chim. Acta* **1990**, *77*, 123.
(39) See http://www.ipc.uni-karlsruhe.de/tch/tch1/index.de.html, Turbomole basis set library, version 5.6, 2004.
(40) Godbout, N.; Salahub, D. R.; Andzelm, J.; Wimmer, E. *Can. J. Chem.* **1992**, *70*, 560.
(41) Perdew, J. P.; Wang, Y. *Phys. Rev. B* **1986**, *33*, 8822.
(42) Becke, A. D. *Phys. Rev. A* **1988**, *38*, 3098.
(43) Becke, A. D. *J. Chem. Phys.* **1993**, *98*, 5648.
(44) Stephens, P. J.; Devlin, F. J.; Chabalowski, C. F.; Frisch, M. J. *J. Phys. Chem.* **1994**, *98*, 11623.
(45) Lee, C.; Yang, W.; Parr, R. G. *Phys. Rev. B* **1988**, *37*, 785.
(46) Becke, A. D. *J. Chem. Phys.* **1993**, *98*, 1372.
(47) (a) Eichkorn, K.; Treutler, O.; Öhm, H.; Häser, M.; Ahlrichs, R. *Chem. Phys. Lett.* **1995**, *240*, 283. (b) Eichkorn, K.; Weigend, F.; Treutler, O.; Ahlrichs, R. *Theor. Chem. Acc.* **1997**, *97*, 199.
(48) Malkin, V. G.; Malkina, O. L.; Reviakine, R.; Arbouznikov, A. V.; Kaupp, M.; Schimmelpfennig, B.; Malkin, I.; Helgaker, T.; Ruud, K.; *MAG-ReSpect*, version 1.2, 2004.
(49) Hess, B. A.; Marian, C. M.; Wahlgren, U.; Gropen, O. *Chem. Phys. Lett.* **1996**, *251*, 365.
(50) Schimmelpfennig, B. *Atomic Meanfield Spin-Orbit Program AMFI*; Stockholms Universitet: Sweden, 1996.
(51) (a) Reed, A. E.; Weinhold, F. *J. Chem. Phys.* **1985**, *83*, 1736. (b) Reed, A. E.; Curtiss, L. A.; Weinhold, F. *Chem. Rev.* **1988**, *88*, 899.
(52) Glendening, E. D.; Badenhoop, J. K.; Reed, A. E.; Carpenter, J. E.; Weinhold, F. *NBO4.M*, version of NBO analysis programs, Theoretical Chemistry Institute, University of Wisconsin, Madison, WI, 1999.
(53) Reviakine, R.; Kaupp, M. Unpublished results, Würzburg 2004.
(54) Mulliken, R. S. *J. Chem. Phys.* **1955**, *23*, 1841.
(55) Flükiger, P.; Lüthi, H. P.; Portmann, S.; Weber, J. *Molekel 4.0*; Swiss Center for Scientific Computing: Manno, Switzerland, 2000. See, e.g.: Portmann, S.; Lüthi, H. P. *Chimia* **2000**, *54*, 766.

Table 1. Selected Bond Lengths (Å) for [Ru(acac)$_2$(L$_{NO}$)] Complexes[a]

state	Ru–O	Ru–N	C1–N	C6–O	C1–C6	C1–C2	C2–C3	C3–C4	C4–C5	C5–C6
neutral exp.	*2.045*	*1.906*	*1.340*	*1.291*	*1.439*	*1.411*	*1.345*	*1.409*	*1.363*	*1.424*
neutral singlet	2.070	1.931	1.355	1.296	1.459	1.425	1.389	1.431	1.391	1.428
neutral triplet	2.018	1.986	1.364	1.326	1.448	1.418	1.401	1.416	1.404	1.413
anion	2.082	1.975	1.371	1.324	1.453	1.419	1.406	1.415	1.408	1.418
cation	2.039	1.966	1.343	1.303	1.466	1.430	1.382	1.440	1.386	1.424
L[b]			1.31	1.22	1.48	1.43	1.34	1.45	1.34	1.43
L^{-} [b]			1.35	1.30	1.43	1.42	1.36	1.42	1.36	1.42
L^{2-} [b]			1.38	1.34	1.42	1.41	1.39	1.41	1.39	1.41

[a] UDFT results with BP86 functional. See Figure 1 for atom labels. Experimental structure parameters for neutral complex from ref 9. [b] Typical average bond lengths in metal-bound *o*-quinonoid ligands.[58]

Table 2. Selected Bond Lengths (Å) for [Ru(acac)$_2$(L$_{NS}$)] Complexes[a]

state	Ru–S	Ru–N	C1–N	C6–S	C1–C6	C1–C2	C2–C3	C3–C4	C4–C5	C5–C6
neutral singlet	2.328	1.943	1.355	1.727	1.448	1.431	1.387	1.427	1.392	1.421
neutral triplet	2.313	1.976	1.366	1.763	1.437	1.422	1.399	1.412	1.405	1.407
anion	2.358	1.982	1.366	1.754	1.445	1.427	1.400	1.417	1.406	1.413
cation	2.318	1.959	1.350	1.723	1.451	1.432	1.384	1.431	1.391	1.418
L[b]			1.31	1.69	1.48	1.43	1.34	1.45	1.34	1.43
L^{-} [b]			1.35	1.72	1.43	1.42	1.36	1.42	1.36	1.42
L^{2-} [b]			1.38	1.75	1.42	1.41	1.39	1.41	1.39	1.41

[a] UDFT results with BP86 functional See Figure 1 for atom labels. [b] Typical average bond lengths in metal-bound *o*-quinonoid ligands.[58]

spin-down component belonging to a given formally doubly occupied MO.[56]

3. Results and Discussion

Molecular Structures. Tables 1 and 2 show optimized structure parameters for the neutral, oxidized (monocationic), and reduced (monoanionic) states of [Ru(acac)$_2$(L$_{NO}$)] and [Ru(acac)$_2$(L$_{NS}$)], respectively, at one particular computational level (BP86). Calculations with hybrid functionals give somewhat longer metal−ligand bonds and correspondingly shorter C1−N and C6−O/S bonds, whereas the remaining intraligand structure parameters change relatively little. Table S1 in Supporting Information provides Cartesian coordinates at all levels used, also for the remaining systems with L$_{OO}$, L$_{NN}$, and L$_{SS}$ ligands (including **g**-tensor orientations).

The ground state of the EPR-silent neutral complex might, in principle, be either a closed-shell singlet or an antiferromagnetically coupled open-shell singlet. We have also optimized the structure of the lowest triplet excited state. Calculations for the singlet did not provide convincing evidence for a broken-symmetry open-shell state. Any spin-polarized solution was at best marginally stabilized compared to the closed-shell wave function. The triplet states were computed to be 17.5 kJ mol^{-1} and 11.8 kJ mol^{-1} higher in energy than the singlet states for [Ru(acac)$_2$(L$_{NO}$)] and [Ru(acac)$_2$(L$_{NS}$)], respectively. This preference for a closed-shell singlet ground state in the neutral systems may be rationalized by a strong coupling between the singly occupied MO (SOMO) of an *o*-semiquinone-type ligand[57] with a suitable singly occupied π-type d-orbital of a Ru^{III} center. We have identified this pairing clearly in the HOMO-2 (third highest doubly occupied MO) of the neutral closed-shell singlet states. Further discussions of the electronic structure of the complexes will be provided below (see also isosurface plots of the most important MOs in Figure S1 in Supporting Information).

For [Ru(acac)$_2$(L$_{NO}$)], that we may compare to an experimental X-ray structure, the calculated intraligand and Ru−ligand distances of the closed-shell singlet appear systematically somewhat too long (by ca. 0.01−0.04 Å at BP86 level; Table 1). The obtained accuracy is similar to results obtained in a very recent, independent DFT study of related complexes of Co and Ni with *o*-quinonoid ligands.[20] Computed distances for the lowest excited triplet state deviate in a nonsystematic way from the experimental ground-state data. For example *d*(Ru−O) is 0.027 Å shorter and *d*(Ru−N) 0.08 Å longer than the experimental value (similar deviations hold also for the intraligand distances). Except for the naturally longer Ru−S and S−C distances in [Ru(acac)$_2$(L$_{NS}$)], the computed dimensions for singlet and triplet states of this complex (Table 2) agree well with the L$_{NO}$ results.

A survey of structural data for *o*-quinonoid ligands by Bhattacharya et al.[58] suggests the assignment of specific average bond lengths to the different ligand oxidation states (see entries in Tables 1, 2). Following this procedure, Patra et al.[9] described the neutral EPR-silent [Ru(acac)$_2$(L$_{NO}$)] as a d^5-Ru^{III} complex with an anionic semiquinone ligand (Ru^{III}/L$^-$). The optimized distances for the singlet state would seem to fit this description (however, see discussion further below).

The Ru−O and Ru−S distances for the cations are somewhat contracted, and the Ru−N distances are expanded by similar amounts. Intraligand distances differ by less than 0.01 Å from the corresponding neutral singlet structures (Tables 1, 2; see also Table S1), which would suggest again a semiquinone ligand. However, the Ru^{IV} center required for this assignment conflicts with chemical intuition, and with the assignment of the EPR data[9] as being due to Ru^{III}/L^0.

---

(56) Kaupp, M.; Asher, J.; Arbuznikov, A.; Patrakov, P. *Phys. Chem. Chem. Phys.* **2002**, *4*, 5458.

(57) Wheeler, D. E.; Rodriguez, J. H.; McCusker, J. K. *J. Phys. Chem. A* **1999**, *103*, 4101.

(58) Bhattacharya, S.; Gupta, P.; Basuli, F.; Pierpont, C. G. *Inorg. Chem.* **2002**, *41*, 5810.

Table 3. Dependence of Total and SOMO Mulliken Spin Densities ($\rho_{\alpha-\beta}$ and ρ_{SOMO}) on the Exchange-Correlation Functional[a]

fragment:		Ru		L		acac1		acac2	
ligand (state)	functional	$\rho_{\alpha-\beta}$	ρ_{SOMO}	$\rho_{\alpha-\beta}$	ρ_{SOMO}	$\rho_{\alpha-\beta}$	ρ_{SOMO}	$\rho_{\alpha-\beta}$	ρ_{SOMO}
L_{NO} (anion)	BP86	0.49	0.31	0.53	0.62	0.00	0.03	0.00	0.03
	B3LYP	0.50	0.20	0.52	0.76	0.00	0.02	0.00	0.02
	BHLYP	0.51	0.10	0.51	0.89	0.00	0.00	0.00	0.00
L_{NS} (anion)	BP86	0.51	0.33	0.47	0.60	0.02	0.03	0.01	0.03
	B3LYP	0.56	0.21	0.44	0.76	0.01	0.01	0.01	0.01
	BHLYP	0.68	0.11	0.30	0.88	0.01	0.00	0.01	0.00
L_{NO} (cation)	BP86	0.76	0.38	−0.07	0.08	0.16	0.28	0.16	0.26
	B3LYP	0.94	0.21	−0.22	0.04	0.14	0.40	0.14	0.35
	BHLYP	0.91	0.09	−0.03	0.01	0.07	0.51	0.06	0.39
L_{NS} (cation)	BP86	0.70	0.36	0.03	0.18	0.15	0.24	0.14	0.22
	B3LYP	0.94	0.21	−0.21	0.14	0.13	0.34	0.14	0.30
	BHLYP	0.94	0.09	−0.10	0.01	0.07	0.51	0.07	0.38

[a] Spin densities broken down into fragment contributions from metal and ligands. See Table S2 in Supporting Information for the other complexes studied.

Compared to the singlet state of the neutral system, the anions exhibit expanded C1−N, C6−O (C6−S), and C4−C5 bonds, and contracted C1−C6 and C3−C4 bonds. It is tempting to take this as indication for a catecholate state of the ligand (and correspondingly for $\mathrm{Ru^{III}}$), which is this time in good agreement with the spectroscopic assignments (but see below). The Ru−ligand bonding distances are all somewhat expanded. Notably, however, the intraligand distances are close to those for the triplet states of the neutral complexes (which is better described by ferromagnetic coupling between $\mathrm{Ru^{III}}$ and $\mathrm{L^-}$; see below). These results show that an unambiguous assignment of metal oxidation state based on computed intraligand structural parameters alone is difficult and appears partly contradictory. Further information is required. We note that the significance of structural parameters in these types of ligands for the determination of physical oxidation states of the metal may vary from high to rather low, depending on a number of factors.[4,59] While assignments of “physical oxidation states” based on structures may be rather accurate for 3d-type complexes,[20] the strong mixing between metal and ligand orbitals appears to render structural information alone less informative for the present Ru systems.

Spin-Density Analyses. In the following we use detailed analyses of spin-density distributions and atomic charges to delineate the electronic structure of the title complexes (we concentrate on the experimentally well-studied complexes with L_{NO} and L_{NS} ligands), and to eventually bracket the physical metal oxidation states. To this end we employ Mulliken atomic spin densities (Table 3) and isosurface plots of the spin-density distributions (Figures 3 and 4), as well as NPA charges (Table 4; see further below). In case of the spin densities we found it mandatory to distinguish between contributions from the singly occupied MO (SOMO) and appreciable spin-polarization contributions from the formally doubly occupied MOs. Spin polarization changes the bonding picture fundamentally, and we analyze it in detail.

Turning first to the two anionic complexes $[\mathrm{Ru(acac)_2(L_{NO})}]^-$ and $[\mathrm{Ru(acac)_2(L_{NS})}]^-$, we see that the Mulliken spin densities (Table 3) indicate a close to equal splitting of the spin between the metal and the quinonoid ligand. The metal spin density increases somewhat with HF exchange contribution, and it is slightly larger for the sulfur-substituted system. Consequently, the spin on the quinonoid ligand decreases from BP86 to B3LYP to BHLYP, and it is slightly lower with L_{NS} than with L_{NO} (Table 3). On the basis of these numbers, we have to assign almost equal weights to descriptions with (a) $\mathrm{Ru^{III}}$ and a dianionic catecholato ligand and with (b) $\mathrm{Ru^{II}}$ and a semiquinone anionic ligand (cf. Scheme 1).

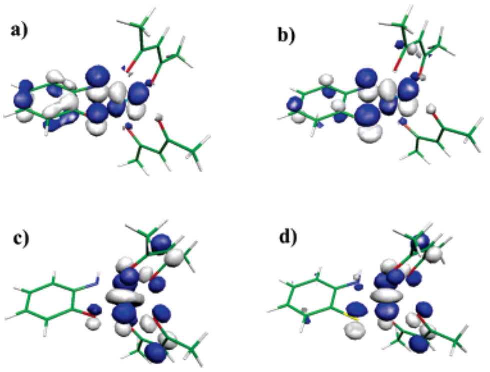

Figure 2. Singly occupied molecular orbitals (SOMO) for (a) $[\mathrm{Ru(acac)_2(L_{NO})}]^-$, (b) $[\mathrm{Ru(acac)_2(L_{NS})}]^-$, (c) $[\mathrm{Ru(acac)_2(L_{NO})}]^+$, and (d) $[\mathrm{Ru(acac)_2(L_{NS})}]^+$ (BP86 results). Isosurfaces ±0.05 au.

Interestingly, however, this description is only obtained after we take the spin polarization contributions into account. The SOMO spin densities are much more localized on the quinonoid ligand and leave relatively little spin on the metal. This becomes even more pronounced with increasing HF exchange admixture to the functional. It is well-known that GGA functionals overestimate metal−ligand bond covalency in transition metal systems, and that HF exchange admixture renders the bonds more ionic.[27,60] Consistent with an M−L antibonding nature of the SOMO (cf. Figure 2), this orbital tends to stay more localized on the ligand along the series of functionals BP86 < B3LYP < BHLYP. Nevertheless, the overall spin on the metal increases along the same series! This must obviously reflect enhanced spin polarization with increasing HF exchange admixture.

These observations are illustrated in more detail in Figure 3. The isosurface plots show the increasing ligand character of the SOMO spin density for both systems with increasing HF exchange admixture. Spin polarization (sum of contributions from all formally doubly occupied MOs to the spin density) develops negative spin density on several ligand atoms, in particular on O/S, C1, C3, C5, and C6. This spin polarization increases notably from BP86 to BHLYP functionals. As a result of compensation between decreasing metal spin density of the SOMO and increasing spin-polarization contributions along this series, the overall metal spin density increases moderately. While this behavior is observed for both anionic complexes, there are also a few differences. In particular, the sulfur atom in L_{NS} develops a large positive SOMO spin density, but also a particularly large negative spin-polarization contribution. Overall, it exhibits a relatively low positive spin density that decreases

---

[59] Sellmann, D.; Binder, H.; Häussinger, D.; Heinemann, F. W.; Sutter, J. *Inorg. Chim. Acta* **2000**, *300*, 829.

[60] See, e.g.: Koch, W.; Holthausen, M. C. *A Chemist’s Guide to Density Functional Theory*; Wiley-VCH: Weinheim, 2000.

Table 4. NPA Charges for Atoms and Fragments[a]

quinonoid ligand L (state of complex)	functional	*Q*(Ru)	*Q*(O/S) (L)	*Q*(N) (L)	*Q*(L) total	*Q*(acac1) total	*Q*(acac2) total
L_{NO} (neutral singlet)	BP86	0.87	−0.54	−0.53	−0.17	−0.36	−0.35
	B3LYP	0.97	−0.59	−0.53	−0.15	−0.43	−0.41
	BHLYP	1.08	−0.64	−0.54	−0.14	−0.49	−0.45
L_{NO} (neutral triplet)	BP86	0.99	−0.56	−0.62	−0.33	−0.38	−0.38
	B3LYP	1.12	−0.61	−0.63	−0.38	−0.38	−0.37
	BHLYP	1.26	−0.69	−0.63	−0.44	−0.40	−0.40
L_{NO} (anion)	BP86	0.82	−0.62	−0.65	−0.71	−0.56	−0.54
	B3LYP	0.91	−0.68	−0.68	−0.78	−0.58	−0.56
	BHLYP	1.05	−0.76	−0.70	−0.86	−0.61	−0.59
L_{NO} (cation)	BP86	1.01	−0.49	−0.51	0.22	−0.12	−0.10
	B3LYP	1.12	−0.52	−0.53	0.27	−0.21	−0.18
	BHLYP	1.25	−0.56	−0.56	0.39	−0.34	−0.31
L_{NS} (neutral singlet)	BP86	0.66	0.15	−0.54	0.06	−0.36	−0.35
	B3LYP	0.77	0.13	−0.56	0.02	−0.40	−0.39
	BHLYP	0.88	0.10	−0.58	−0.01	−0.44	−0.44
L_{NS} (neutral triplet)	BP86	0.76	0.12	−0.62	−0.08	−0.34	−0.34
	B3LYP	0.88	0.10	−0.63	−0.10	−0.42	−0.37
	BHLYP	1.02	0.02	−0.63	−0.11	−0.48	−0.44
L_{NS} (anion)	BP86	0.62	−0.04	−0.65	−0.50	−0.57	−0.56
	B3LYP	0.74	−0.11	−0.68	−0.62	−0.56	−0.55
	BHLYP	0.93	−0.21	−0.74	−0.75	−0.60	−0.60
L_{NS} (cation)	BP86	0.78	0.28	−0.52	0.47	−0.13	−0.12
	B3LYP	0.92	0.28	−0.55	0.50	−0.22	−0.20
	BHLYP	1.10	0.29	−0.57	0.57	−0.36	−0.32

[a] See Table S3 in Supporting Information for the other complexes studied.

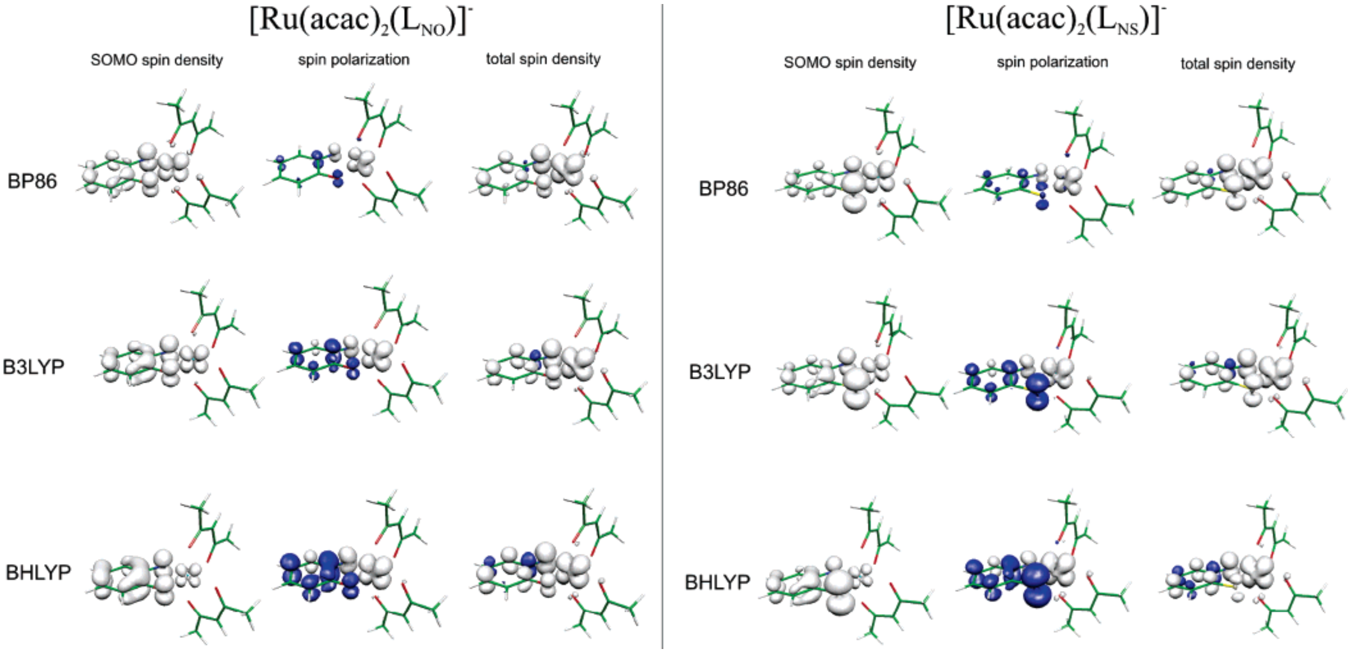

Figure 3. Dependence of spin density distribution and spin polarization on functional for $[Ru(acac)_2(L_{NO})]^-$ and $[Ru(acac)_2(L_{NS})]^-$. Isosurfaces ±0.003 au.

with increasing HF exchange admixture (Figure 3). The isosurface plots demonstrate very clearly the decisive influence of spin polarization on the bonding picture obtained in a single-determinant unrestricted Kohn−Sham framework. Mulliken spin densities for the remaining anions are provided in Table S2 in Supporting Information. While the complexes with $L = L_{OO}$, L_{SS} behave similarly as the two systems discussed, the spin polarization is much less pronounced for L_{NN}, where the resulting spin density remains much more on the quinonoid ligand (ca. 60%) than on the metal (see also isosurface plots in Figure S2 in Supporting Information).

The remarkable importance of spin polarization becomes even more pronounced when we turn to the cationic complexes. The Mulliken spin densities (Table 3, cf. Table S2 in Supporting Information for further data) favor now clearly a metal-centered spin density, consistent with chemical intuition, which would clearly favor a description Ru^{III}/L^0 over Ru^{IV}/L^- (cf. Scheme 1; recall the ambiguous structural description above). However, this distribution is again not reflected at all by the SOMO spin densities, and the result depends somewhat on the functional. The SOMO itself is extensively delocalized. Interestingly, its largest ligand contributions come not from the quinonoid ligand

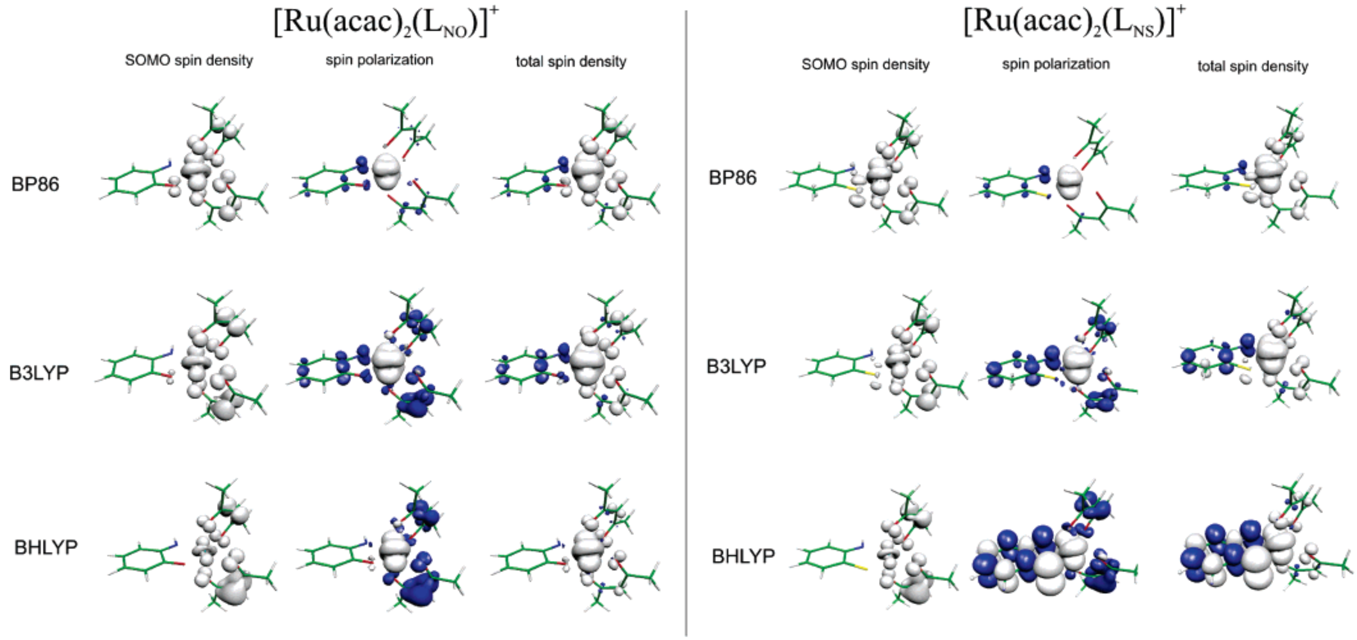

Figure 4. Dependence of spin density distribution and spin polarization on functional for $[Ru(acac)_2(L_{NO})]^+$ and $[Ru(acac)_2(L_{NS})]^+$. Isosurfaces ±0.003 au.

but from the anionic acetylacetonato ligands (this delocalization is unsymmetrical and favors the ligand designated as acac1; cf. Figure 1 and Table 3). The SOMO isosurface plots in Figures 2c and 2d reflect clearly the antibonding nature of the SOMO for the bonds between metal and acac ligands, with only small coefficients on the quinonoid ligand. This leads to the delocalized SOMO spin density in Figure 4. Spin polarization is again dramatic once we include HF exchange into the functional. It provides negative spin-density contributions on both acac ligands. For the complex $[Ru(acac)_2(L_{NS})]^+$, spin polarization affects also the quinonoid ligand, leading now in particular to negative spin densities for the N, C2, C4, and C6 atoms, and to positive spin density on S, C1, C3, and C5. In the overall spin density distribution, the spin polarization reduces the spin on the acac ligands dramatically, and it places some spin on the quinonoid ligand for $[Ru(acac)_2(L_{NS})]^+$ but less so for $[Ru(acac)_2(L_{NO})]^+$ (Figure 4, Table 3). In consequence, a strong dominance of the metal in the spin density distribution is obtained, but only after we have accounted for spin polarization of the doubly occupied MOs.

Despite the different spin density distribution of anionic and cationic complexes, a common basic pattern upon increasing HF exchange in the functional emerges. This is the increasing localization of the SOMO on the ligands (on the quinonoid ligand for the anionic systems and on the acac ligands for the cations), which is overcompensated by dramatically increased spin polarization. In all cases, the overall metal spin density increases somewhat from BP86 to B3LYP. For the anions it increases further from B3LYP to BHLYP whereas it decreases slightly or stagnates for the cations (Table 3). A breakdown of the spin polarization contributions to spin density into dominant contributions from individual orbitals is provided for $[Ru(acac)_2(L_{NO})]^+$ in Figure S3 in Supporting Information. We note in passing that the triplet excited state of the neutral complexes exhibits a similar importance of spin polarization for the total spin density distribution as found for anions and cations, with an enhancement of metal spin density from about 0.65 to 1.03 (cf. Table S2 in Supporting Information).

NPA Charges, Improved Assignments of Formal Oxidation States. When using atomic charges to discuss formal oxidation states, one has to keep in mind that the actual charge distribution in the presence of covalent bonding will inevitably deviate significantly from formal atomic charges corresponding to formal oxidation numbers.[61] One may nevertheless look for trends in computed charges, either with different ligands or in comparing different charge states. Indeed, the NPA charges in Table 4 for neutral, cationic and anionic complexes with L = L_{NO}, L_{NS} provide an interesting picture of how the charge transfer between ligands and metal changes when electrons are added or removed from the system. Together with the spin-density analyses provided above, we may indeed bracket the most realistic formal description for each system in remarkable detail.

The metal NPA charges tend to be in the range of +1 in all cases and increase slightly with increasing HF exchange admixture, as expected.[60] Most interestingly, for a given functional there is a very good match between the metal charges for anions and the closed-shell singlet state of the neutral system (Table 4). The cationic complexes and the triplet state of the neutral complexes also have strikingly similar metal charges, which are larger than for anions and neutral singlet states. Remarkably, this holds at any of the given DFT levels, which gives additional support to the resulting interpretations.

While we obviously cannot derive physical oxidation states directly from computed atomic charges (see above), we may use the charges to cross-check the assignments made on the basis of the spin-density analyses. Recall that the analyses of the spin-density distributions for the cations suggested strongly a Ru^{III} state (with formally neutral L; see above). The close similarity in the metal charges for the cationic complex and the triplet state of the neutral complex suggests then clearly that the triplet state of the neutral complexes is best represented by a ferromagnetic coupling between a d^5-Ru^{III} center and a semiquinone-type ligand. On the other hand, we interpreted the

---

(61) See, e.g.: Kaupp, M.; v. Schnering, H. G. *Angew. Chem.* **1995**, *107*, 1076; *Angew. Chem., Int. Ed. Engl.* **1995**, *34*, 986.

spin-density distributions of the anionic complexes as being intermediate between a description Ru^{II}/L^{-} and Ru^{III}/L^{2-} (see above). But then the singlet ground state of the neutral complexes is also better described as intermediate between Ru^{III} and Ru^{II}, with L being intermediate between L^0 and L^-. This may be rationalized by formal donation of charge density from the SOMO of a semiquinone-type ligand into a metal π-type orbital. Indeed, as discussed further above, the HOMO-2 of the closed-shell singlet state exhibits this type of strong interaction.

The ligand fragment NPA charges (Table 4) confirm our reasoning: The charge on L is most negative for the anionic complexes, where the ligand is thought to be intermediate between L^- and L^{2-}. It is somewhat less negative for the triplet state of the neutral system, where we assign the ligand as close to L^-. The still lower value for the closed-shell singlet corresponds to our description of L as intermediate between L^0 and L^-. Finally, the slightly positive ligand charge on L for the cationic complexes reflects nicely the assignment as L^0. In all cases, the charge on L_{NS} is less negative (more positive) than on L_{NO}, consistent with the lower electronegativity of sulfur compared to oxygen (see also individual charges for the ligand donor atoms in Table 4; the appreciable Ru−S covalency is relevant for the discussion of spin contamination further below). Charges on the acac ligands are generally negative and vary more moderately than on L, consistent with a buffer-type role of these anionic co-ligands. Obviously, the covalency of the metal-acac interactions is least pronounced for the anionic complexes and most pronounced for the cations. NPA charges for complexes with the other ligands provide a similar picture (cf. Table S3 in Supporting Information).

Based on these detailed analyses of spin and charge densities, we therefore have to modify the established interrelations between intramolecular distances and charge state of *o*-quinonoid ligands.[9,58] This holds for the systems studied here, but probably also for many other related complexes. Recall that the X-ray structure of neutral $[Ru(acac)_2(L_{NO})]$ was interpreted as reflecting a Ru^{III}/L^- system.[9] Both experimental and computed intra-ligand distances for the closed-shell singlet ground-state agreed well with the tabulated data[58] for *o*-quinonoid ligands in an L^- monoanionic state. However, our present analyses for the closed-shell singlet suggest a description intermediate between L^- and L^0. It is rather the triplet state of the neutral complexes that corresponds to a relatively clear-cut Ru^{III}/L^- description (see above). We suggest therefore that, after correction for a slight systematic overestimate of distances by the DFT level used (see above), the computed intra-ligand distances for the triplet states in Tables 1,2 should provide a better estimate for metal-bound *o*-quinonoid ligands in a semiquinone state. Similarly, the cationic complexes should provide reasonable reference values for a neutral state of the bound ligands (Tables 1,2).

g-Tensor Values and Orientations. Table 5 compares computed **g**-tensors with the three different density functionals for all five cationic and five anionic complexes, together with the available experimental results for the iminoquinone and iminothioquinone complexes. We provide also for each of the three functionals employed the $\langle S^2 \rangle$ expectation value of the Kohn−Sham determinant as an approximate measure of spin contamination.[62,63] All four experimentally determined **g**-tensors exhibit one component significantly below g_e (g_{11}) and two components appreciably above g_e (Table 5). The latter (g_{22}, g_{33}) have either been reported as equal (for $[Ru(acac)_2(L_{NO})]^-$ and for $[Ru(acac)_2(L_{NS})]^+$), leading to an axially symmetrical tensor, or as different (for $[Ru(acac)_2(L_{NO})]^+$ and for $[Ru(acac)_2(L_{NS})]^-$), leading to a rhombic tensor. In all four examples, the experimentally determined **g**-tensor anisotropy $g_{33} - g_{11}$ is sizable, between 191 and 305 ppt. The isotropic *g*-values are all above g_e, but more so for the cationic than for the anionic complexes.

The computed **g**-tensors (Table 5) exhibit a pronounced dependence on the Hartree−Fock exchange admixture to the exchange-correlation functional. Let us start with the experimentally negative *g*-shift component, Δg_{11}. This is not reproduced at all very well by the calculations. The gradient-corrected BP86 functional provides small negative Δg_{11} for the anions or small positive Δg_{11} for the cations. Admixture of ca. 20% HF exchange with the B3LYP functional improves agreement with experimental Δg_{11} somewhat for the two anionic complexes but leads to even slightly more positive Δg_{11} for the two cationic complexes. Only upon increasing the HF exchange admixture to 50% with the BHLYP functional, Δg_{11} is computed to be negative also for the cations. But it remains appreciably (30−70 ppt) above experiment. While this component is thus rather sensitive to the exchange-correlation functional, we believe that the deviations from experiment reflect in particular the neglect of higher-order relativistic contributions in our present calculations (some of the scalar relativistic effects are included via the Ru ECP). In σ-radicals containing heavy elements, negative parallel *g*-shift components have been attributed either to higher-order SO effects (reproducible in two-component calculations[64]) or to cross-terms with scalar relativistic effects (in Breit−Pauli perturbation analyses[65]). Ligand-field arguments[66] attribute the negative $\Delta g_{\|}$ in low-spin d^5 complexes partly to quadratic SO contributions (as well as to couplings between SOMO and "e_g"-type orbitals,[35] cf. below). Our recent preliminary relativistic two-component calculations on small tetragonal 4d-complexes indicate indeed sizable negative higher-order SO contributions to $g_{\|}$.[67] Future two-component analyses of the title complexes should provide deeper insight into this as yet open question.

Better agreement with experiment may be achieved for the positive Δg_{22} and Δg_{33} components, but only upon inclusion of HF exchange admixture (Table 5). The BP86 calculations provide generally too-low values for these two components, and therefore far too low **g**-tensor anisotropy. HF exchange increases both components. On the basis of the agreement with experiment, it is difficult to choose between the B3LYP and BHLYP functionals in this case: While agreement is excellent with B3LYP for $[Ru(acac)_2(L_{NS})]^+$, the average of the experimental Δg_{22} and Δg_{33} values is in most other cases bracketed by the

---

[62] For the BP86 functional, these $\langle S^2 \rangle$ values pertain to the noninteracting reference system rather than to the real system. For the hybrid functionals, matters are even more complicated, due to the admixture of the nonlocal and nonmultiplicative Hartree−Fock exchange potential (see Arbuznikov, A. V.; Kaupp, M. *Chem. Phys. Lett.* **2004**, *391*, 16, for a proper localized implementation of hybrid potentials for **g**-tensor calculations). Such data are nevertheless expected to give a reasonable and useful measure of spin contamination (see, e.g., Baker, J.; Scheiner, A.; Andzelm, J. *Chem. Phys. Lett.* **1993**, *216*, 380). In our experience, large spin contamination of the Kohn−Sham calculation signals problems also for EPR parameter calculations (see, e.g., ref 63).

[63] Munzarová, M. L.; Kaupp, M. *J. Phys. Chem. A* **1999**, *103*, 9966.

[64] Patchkovskii, S.; Schreckenbach, G. *Calculation of EPR g-Tensors by Density Functional Theory*. In ref 33, Chapter 32, pp 513−540.

[65] Manninen, P.; Vaara, J.; Ruud, K. *J. Chem. Phys.* **2004**, *121*, 1258.

[66] Atkins, P. W.; Jamieson, A. M. *Mol. Phys.* **1967**, *14*, 425.

[67] Malkin, I.; Malkina, O. L.; Malkin, V. G., Kaupp, M. Unpublished results.

Table 5. Computed and Experimental **g**-Tensors[a]

		BP86	B3LYP	BHLYP	exp.[9]
$[Ru(acac)_2(L_{NO})]^-$	g_{iso}	2.0111 (8.8)	2.0239 (21.6)	2.0339 (31.6)	2.026 (23.7)
	g_{11}	1.9852 (−17.1)	1.9649 (−37.4)	1.9330 (−69.3)	1.8870 (−115.3)
	g_{22}	2.0148 (12.4)	2.0404 (38.0)	2.0597 (57.4)	2.0922 (89.9)
	g_{33}	2.0333 (31.0)	2.0664 (64.1)	2.1091 (106.8)	2.0922 (89.9)
	$g_{33}-g_{11}$	0.0481	0.1015	0.1761	0.2052
	$\langle S^2\rangle^b$	0.755	0.759	0.774	
$[Ru(acac)_2(L_{NS})]^-$	g_{iso}	2.0084 (6.1)	2.0260 (23.7)	2.0666 (64.3)	2.027 (24.7)
	g_{11}	1.9845 (−17.8)	1.9659 (−36.4)	1.9215 (−80.8)	1.8895 (−112.8)
	g_{22}	2.0034 (1.1)	2.0394 (37.1)	2.1206 (118.3)	2.0735 (71.2)
	g_{33}	2.0374 (35.1)	2.0727 (70.4)	2.1576 (155.3)	2.111 (108.6)
	$g_{33}-g_{11}$	0.0529	0.1068	0.2361	0.2215
	$\langle S^2\rangle^b$	0.755	0.760	0.770	
$[Ru(acac)_2(L_{OO})]^-$	g_{iso}	2.0338 (31.5)	2.0649 (62.6)	2.1646 (162.3)	
	g_{11}	2.0019 (−0.4)	2.0082 (5.9)	2.0221 (19.8)	
	g_{22}	2.0320 (29.6)	2.0797 (77.4)	2.1822 (179.9)	
	g_{33}	2.0676 (65.2)	2.1069 (104.5)	2.2894 (287.0)	
	$g_{33}-g_{11}$	0.0657	0.0987	0.2673	
	$\langle S^2\rangle^b$	0.754	0.758	0.760	
$[Ru(acac)_2(L_{NN})]^-$	g_{iso}	1.9910 (−11.3)	1.9953 (−7.0)	1.9846 (−17.7)	
	g_{11}	1.9747 (−27.7)	1.9895 (−12.8)	1.9773 (−25.0)	
	g_{22}	1.9941 (−8.2)	1.9966 (−5.7)	1.995 (−7.0)	
	g_{33}	2.0043 (2.0)	1.9998 (−2.5)	1.9811 (−21.2)	
	$g_{33}-g_{11}$	0.0296	0.0103	0.0181	
	$\langle S^2\rangle^b$	0.755	0.761	0.782	
$[Ru(acac)_2(L_{SS})]^-$	g_{iso}	2.0283 (25.9)	2.0698 (67.4)	2.1448 (142.5)	
	g_{11}	2.0117 (9.4)	2.0431 (40.8)	2.0422 (39.9)	
	g_{22}	2.0347(32.4)	2.0508 (48.5)	2.1151 (112.7)	
	g_{33}	2.0384 (36.1)	2.1154 (113.1)	2.2771 (274.8)	
	$g_{33}-g_{11}$	0.0267	0.0723	0.2349	
	$\langle S^2\rangle^b$	0.754	0.757	0.761	
$[Ru(acac)_2(L_{NO})]^+$	g_{iso}	2.0672 (64.9)	2.1079 (105.6)	2.1771 (174.8)	2.103 (100.7)
	g_{11}	2.0058 (3.4)	2.0152 (12.5)	1.9909 (−11.8)	1.9232 (−79.1)
	g_{22}	2.0883 (85.9)	2.1332 (130.5)	2.2526 (249.9)	2.1468 (144.5)
	g_{33}	2.1076 (105.3)	2.1754 (172.6)	2.2879 (285.1)	2.2278 (225.5)
	$g_{33}-g_{11}$	0.1018	0.1602	0.2970	0.3046
	$\langle S^2\rangle^b$	0.771	0.834	0.762	
$[Ru(acac)_2(L_{NS})]^+$	g_{iso}	2.0703 (68.0)	2.1081 (105.7)	2.1786(176.3)	2.094 (91.7)
	g_{11}	2.0118 (9.5)	2.0245 (22.2)	1.9997 (−2.6)	1.9645 (−37.8)
	g_{22}	2.0893 (87.0)	2.1400 (137.7)	2.2537 (251.4)	2.156 (153.7)
	g_{33}	2.1098 (107.5)	2.1597 (157.3)	2.2824 (280.1)	2.156 (153.7)
	$g_{33}-g_{11}$	0.0980	0.1352	0.2827	0.1915
	$\langle S^2\rangle^b$	0.766	0.855	1.289	
$[Ru(acac)_2(L_{OO})]^+$	g_{iso}	2.0728 (70.5)	2.1215 (119.2)	2.1803 (178.0)	
	g_{11}	2.0166 (14.3)	2.0410 (38.6)	1.9944 (−7.9)	
	g_{22}	2.0784 (76.1)	2.1253 (123.0)	2.2615(259.2)	
	g_{33}	2.1235(121.1)	2.1983 (196.0)	2.2849 (282.6)	
	$g_{33}-g_{11}$	0.1069	0.1573	0.2905	
	$\langle S^2\rangle^b$	0.809	1.001	0.762	
$[Ru(acac)_2(L_{NN})]^+$	g_{iso}	2.0625 (60.2)	2.0980 (95.6)	2.1646 (162.3)	
	g_{11}	2.0019 (−0.4)	2.0032 (0.8)	1.9912 (−11.1)	
	g_{22}	2.0761 (73.8)	2.1321 (129.8)	2.2205(218.2)	
	g_{33}	2.1094 (107.1)	2.1587 (156.3)	2.2821 (279.8)	
	$g_{33}-g_{11}$	0.1075	0.1555	0.2909	
	$\langle S^2\rangle^b$	0.762	0.788	0.764	
$[Ru(acac)_2(L_{SS})]^+$	g_{iso}	2.0697 (67.3)	2.1044 (102.0)	2.1551 (152.8)	
	g_{11}	2.0145 (12.1)	2.0409 (38.6)	1.9769 (−25.5)	
	g_{22}	2.0874 (85.1)	2.1320 (129.7)	2.2201 (217.7)	
	g_{33}	2.1072 (104.9)	2.1401 (137.8)	2.2684 (266.1)	
	$g_{33}-g_{11}$	0.0927	0.0992	0.2915	
	$\langle S^2\rangle^b$	0.768	0.975	1.556	

[a] Absolute *g*-values with *g*-shifts in ppt in parentheses. [b] Expectation value for the Kohn−Sham determinant.

B3LYP and BHLYP data. Taking the poorly reproduced Δg_{11} into account, the large **g**-tensor anisotropy is mostly better reproduced by the BHLYP functional. But this may be a fortuitous result (see above). In contrast, the B3LYP functional provides then generally the best agreement with experiment for g_{iso}, whereas BHLYP tends to give too-large isotropic values. In the case of $[Ru(acac)_2(L_{NS})]^+$, BHLYP overshoots Δg_{22} and Δg_{33} significantly and gives thus also a far too large anisotropy. In this case the “half-and-half functional” is also plagued by substantial spin contamination (cf. $\langle S^2\rangle$ value in Table 5), whereas spin contamination is generally small for the anionic systems and is moderate for $[Ru(acac)_2(L_{NO})]^+$ (see also below).

Presuming that the relatively large negative Δg_{11} values are partly caused by higher-order relativistic effects (see above), one might conclude that a functional with HF exchange admixture between that of B3LYP and BHLYP should provide the best agreement with experiment. This is consistent with similar results for typical 3d-complexes,[32,68] as well as for $4d^1$ Mo(V) systems.[69] If we take the increase of the three tensor components from the anionic to the corresponding cationic complex as a good measure, the B3LYP results appear much more reasonable than the BHLYP data, which largely overestimate this difference (in the comparison, we have chosen to average the g_{22} and g_{33} values, see below). Differences between g_{33} and g_{22} appear to be difficult to reproduce. In some cases they depend appreciably on the functional, and sometimes the results deviate strongly from experiment (which on the other hand may not always be reliable for this quantity).

The **g**-tensor calculations are obviously still far from the predictive accuracy that they provide already for purely organic radicals. We may have to provide both improved treatments of exchange and correlation, as well as inclusion of higher-order relativistic contributions, before we may reach comparable accuracy as is already possible[70] for, e.g., bioradicals. Despite their limited quantitative accuracy, the computed **g**-tensors reproduce well some of the experimental trends, that is the larger isotropic g-values and **g**-tensor anisotropies of the cationic compared to the anionic complexes. This is consistent with a larger spin density on the metal for the oxidized complexes, in agreement with the spin-density analyses provided above. On the other hand, even for the anionic complexes, the **g**-anisotropies may only be rationalized by appreciable spin density on the metal. The axial symmetry (equality between g_{22} and g_{33}) for $[\mathrm{Ru(acac)_2(L_{NO})}]^-$ and $[\mathrm{Ru(acac)_2(L_{NS})}]^+$ is reproduced by none of the functionals. Even if we take into account a possible lack of resolution in the experimental determination of these two components at X-band,[9] this observation arises from the relatively complicated electronic structure of the complexes (see analyses further below).

Computed **g**-tensors for systems with $\mathrm{L_{SS}}$, $\mathrm{L_{OO}}$, and $\mathrm{L_{NN}}$ are also provided in Table 5. In the absence of experimental data for these complexes, we may analyze in particular differences relative to the corresponding experimentally known systems. For the anionic complexes with $\mathrm{L_{OO}}$ and $\mathrm{L_{SS}}$ ligands, the calculations predict somewhat larger (more positive, less negative) values for all three tensor components compared to the systems with $\mathrm{L_{NO}}$ and $\mathrm{L_{NS}}$. In contrast to the latter two complexes, increasing HF exchange admixture makes now all three components more positive. The anionic complex with $\mathrm{L_{NN}}$ exhibits unexpectedly two appreciably negative tensor components and one closer to g_e (three negative g-shift components with BHLYP). Computed **g**-tensor components for the cationic complexes provide an overall more uniform impression along the series of five ligands (Table 5). The tensors are similar in having two positive and one negative (or small positive) component showing in all cases the same tendencies as described for $\mathrm{L_{NO}}$ and $\mathrm{L_{NS}}$.

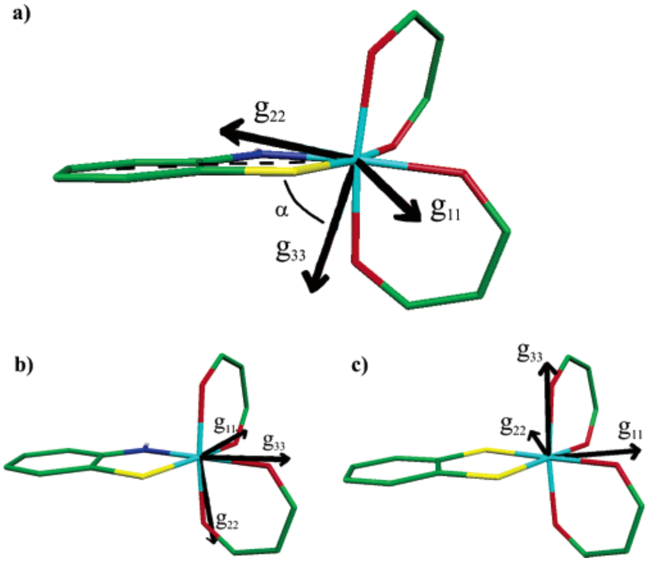

Figure 5. Computed orientation of **g**-tensors (B3LYP functional). (a) Cationic complexes (as example $[\mathrm{Ru(acac)_2(L_{NS})}]^+$). The angle α indicates the deviation of the largest tensor component, g_{33}, from the bisector of the M−L chelate bond angle. (b) For $[\mathrm{Ru(acac)_2(L_{NO})}]^-$ and $[\mathrm{Ru(acac)_2(L_{NS})}]^-$. (c) For $[\mathrm{Ru(acac)_2(L_{OO})}]^-$ and $[\mathrm{Ru(acac)_2(L_{SS})}]^-$. The orientation for $[\mathrm{Ru(acac)_2(L_{NN})}]^-$ results by exchanging g_{33} and g_{11}

Tensor orientations are not known experimentally for any of the systems studied here but provide additional insight into relations between **g**-tensor and electronic structure. Representative predicted orientations are indicated in Figure 5 (the tensor principal axes are included also in the coordinate sets in Table S1 in Supporting Information). As the situation is more straightforward for the cations than for the anions, we start the discussion with the former. As indicated in Figure 5a, the smallest (experimentally negative) g_{11} component for all cations points parallel to the quinonoid ligand plane but perpendicular to the bisector of the chelate bite angle of this ligand. However, the orientations of the largest component g_{33} and the middle component g_{22} vary within the plane to which g_{11} stands perpendicular. We may express these orientations via the angle α of g_{33} to the ligand plane (Figure 5a): With $\mathrm{L_{NO}}$, α is −13.5°, i.e., g_{33} points slightly below the ligand plane. In contrast, the angle α is −57.3° with $\mathrm{L_{NS}}$. With the more symmetrical ligands, g_{33} is either directly within the plane ($\alpha = 0°$, with $\mathrm{L_{OO}}$) or exactly perpendicular to it ($\alpha = -90°$, with $\mathrm{L_{NN}}$ and $\mathrm{L_{SS}}$). These different rotations of g_{33} and g_{22} may be understood from the π-donor character of L (see below). Notably, the orientations do not depend much on the exchange-correlation functional for the cations (the BP86 axes differ slightly from the results with hybrid functionals, on which Figure 5 is based).

The situation is more complicated for the anions, where we have to distinguish different cases (Figure 5b,c). The dependence to the functional is slightly more pronounced than for the cations, but the general trends are unchanged. We will refer to the results obtained with the B3LYP functional which provide the intermediate orientation. The orientation with $\mathrm{L} = \mathrm{L_{NO}}$, $\mathrm{L_{NS}}$ is indicated in Figure 5. The largest component, g_{33}, points roughly along the N−Ru bond, g_{22} is almost perpendicular to the quinonoid ligand plane, and g_{11} is roughly along the O−Ru/S−Ru bond of the quinonoid ligand. With $\mathrm{L} = \mathrm{L_{OO}}$, $\mathrm{L_{SS}}$ (Figure 5c), g_{33} points almost exactly perpendicular to the ligand plane, g_{11} is oriented exactly along the bisector of the chelate ligand

---

(68) Remenyi, C.; Munzarová, M. L.; Kaupp, M. *J. Phys. Chem. B* **2005**, *109*, 4227.

(69) Fritscher, J.; Hrobarik, P.; Kaupp, M. Unpublished results.

(70) Kaupp, M. EPR Spectroscopy of Free Radicals in Solids. Trends in Methods and Applications. In *Progress in Theoretical Chemistry and Physics*; Lund, A., Shiotani, M., Eds.; Kluwer: Dordrecht, 2003; Vol. 10, p 267.

bite angle of L, and g_{22} is in the plane but perpendicular to the bisector. Compared to these two cases, we have to exchange g_{33} and g_{11} for L_{NN} (Figure 5c). These rather different magnetic axes suggest an appreciable influence of the exact nature of the quinonoid ligand on electronic structure and **g**-matrix.

Analysis of g-Tensors. To better understand the relation of the computed **g**-tensors to electronic structure and spin density, we have made use of two analysis tools available within MAG-ReSpect:[48] (a) The atomic nature of both SO-ECP and atomic meanfield SO operators h_{SO} allows us to break down the dominant $\Delta\mathbf{g}^{SO/OZ}$ part of the *g*-shift tensor (eq 3) into atomic contributions by switching SO operators on or off for individual atoms or groups of atoms.[28] (b) We may decompose $\Delta\mathbf{g}^{SO/OZ}$ into individual couplings ("excitations") between an occupied and a vacant MO within the sum-over-states expression (eq 3).[56] This is particularly easy for nonhybrid functionals (here the BP86 GGA), where the equations are not coupled by HF exchange terms.

The atomic analyses (provided in Tables S4 and S5 in Supporting Information) show clearly the dominance of ruthenium SO coupling in all **g**-tensors. Contributions from the acac ligands range from completely negligible for the anions to about 2−3 ppt for Δg_{33} in the cations. This is consistent with the partial delocalization of the SOMO onto the acac ligands for the cations (cf. Table 4 and Figure 4 above). Contributions from the quinonoid ligand L are somewhat larger, in particular, when heavier sulfur donor atoms with larger SO coupling constants are involved ($L = L_{NS}$, L_{SS}). In this case the interplay between spin delocalization and spin polarization (see above) leads to a complicated dependence of the sulfur SO contributions to Δg_{33} on the exchange-correlation functional. They decrease somewhat when going from BP86 to BHLYP for the anionic complexes (from ca. 6 ppt to ca. 3 ppt for $[Ru(acac)_2(L_{NS})]^-$ and from sizable ca. 16 to ca. 13 ppt for $[Ru(acac)_2(L_{SS})]^-$). This correlates with decreasing spin density on L with increasing HF exchange admixture (both total spin density and SOMO spin density, cf. Table 4). For the cationic systems a more irregular behavior is seen, with a sudden jump of sulfur contributions to Δg_{33} from 3 to 9 ppt for BP86 and B3LYP up to more than 30 ppt for BHLYP (Table S5). This is undoubtedly related to the increasing spin contamination for these cationic complexes at BHLYP level (cf. Table 3) and to the related large spin-polarization contribution to a positive sulfur spin density (cf. Figure 4). In any case, the metal SO contribution determines predominantly the **g**-tensor for both anions and cations.

The precise form of the tensor is in turn controlled by the nature of the SOMO, which differs substantially for anionic and cationic complexes (cf. Figure 2). While it is an out-of-plane π-antibonding combination between metal and quinonoid ligand for the anions, it is of more in-plane metal d-orbital type (relative to the plane of L), with M-acac π-antibonding character for the cations. Consequently, the orientation of the tensors differs for anions and cations (cf. Figure 5). The **g**-tensors for the cations may be understood somewhat more easily, and we will discuss them first before turning to the more complicated anions.

Once we disregard the strong influence of spin polarization on the oxidation-state assignment Ru^{III}/L^0 for the cations (see above), these systems are properly described as distorted octahedral low-spin d^5 systems. The obvious starting points for analysis are thus ligand-field theory (LFT) arguments, which are well established for the low-spin d^5 case.[35,71] A very basic LFT treatment would neglect any charge transfer from the ligands and even any couplings to those levels derived from the e_g set of orbitals in an exactly octahedral system (but see below). Then only excitations within the approximate t_{2g} set are considered (this pertains thus only to the second sum over β-orbitals in eq 3, and one expects mainly positive *g*-shifts). For a symmetry lower than O_h, the formal degeneracy within this set is lifted.[72] Looking already beyond LFT, we expect the three MOs to be ordered such that the MO with the largest metal−ligand π-antibonding interactions is highest in energy and thus becomes the SOMO (the HOMO has intermediate π-antibonding character and the HOMO−1 the lowest).[71b] LFT would suggest that couplings between HOMO and SOMO will dominate g_{33} and the coupling between HOMO−1 and SOMO will dominate g_{22}. This is in some cases borne out by our excitation analyses of the computed **g**-tensors, but the situation is more complex. The SOMO is in all cations mainly of π-antibonding character of the metal with the acac ligands (cf. Figure 2), which represent the strongest π-donors. The HOMO is generally somewhat π-antibonding to acac ligands and partly to L, and it differs most from system to system (cf. Figure S1 in Supporting Information). The M−L π-antibonding character of the HOMO is small on nitrogen, larger on oxygen, and largest on sulfur. In contrast, some nitrogen π-antibonding contributions are visible for the HOMO−1 (Figure S1). The π-donor character of the different donor atoms of L influences the orientations of g_{33} and g_{22} to some extent (Figure 5), as the couplings between HOMO and SOMO and between HOMO−1 and SOMO contribute mainly to the component closest and farthest from the ligand plane, respectively. Overall, the couplings from doubly occupied MOs and SOMO (double-SOMO couplings) for L_{NO}, L_{NS}, L_{NN}, and L_{SS}, respectively, sum up to about +150, +133, +138, and +140 ppt to the component closer to the plane, and to about +83, +98, + 99, and +83 ppt to the more perpendicular component (the analysis for L_{OO} was hampered by the too strong spin polarization which did not allow a proper matching of α- and β-MOs). This alone would not yet explain the different tensor orientations. At the same time, one has to take into account also couplings between SOMO and virtual MOs (this pertains to the first sum over α-orbitals in eq 3). These excitations, which are sometimes neglected in basic LFT approaches (but see ref 34), are non-negligible for all three tensor components and influence also the orientations of g_{33} and g_{22}. In particular, couplings with one or two metal−ligand antibonding orbitals of "e_g" type (LUMO+1 and LUMO+2 for L_{NO}, L_{NS}, LUMO+2 for L_{NN}, and LUMO+1 for L_{SS}; cf. Figure S1) make large negative contributions of ca. −40 to −50 ppt to that of the two components which is closer to the plane of the ligand. Good π-donors such as L_{SS} reduce the ligand-field splittings between levels derived from the t_{2g} and e_g sets by destabilizing the "t_{2g}"-type orbitals. They thereby enhance the negative contributions. Additional contributions from SOMO−LUMO coupling contribute *positively* to the more perpendicular

---

[71] (a) McGarvey, B. R. *Coord. Chem. Rev.* **1998**, *170*, 75. (b) Neese, F.; Zaleski, J. M.; Loeb Zaleski, K.; Solomon, E. I. *J. Am. Chem. Soc.* **2000**, *122*, 11703. (c) Shokirev, N. V.; Walker, F. A. *J. Am. Chem. Soc.* **1998**, *120*, 981. (d) Raitsimring, A. M.; Walker, F. A. *J. Am. Chem. Soc.* **1998**, *120*, 991. (e) Stratemeier, H.; Hitchmann, M. A.; Comba, P.; Bernhardt, P.; Riley, M. J. *Inorg. Chem.* **1991**, *30*, 4088.

[72] The relatively low symmetry in the complexes studied here lifts the degeneracy substantially. This justifies the use of perturbation theory as applied in this study.

component (about +10, +22, +21, and +28 ppt for L_{NO}, L_{NS}, L_{NN}, and L_{SS}, respectively). As these contributions arise from the first part of eq 3, the positive values indicate a negative sign of the product of spin−orbit and orbital−Zeeman matrix elements. This points to a large off-center character of the SOMO−LUMO coupling.[73] This is part of the difficulty for these d^5 cations, but also for the anions: For early transition metal complexes with low d-electron count (e.g. d^1 complexes[27,68,69] such as V^{IV} or Mo^{V}), one expects negative *g*-shift components, due to the dominance of couplings between SOMO and virtual MOs. In very late transition metal complexes (e.g. d^9-Cu^{II}), the couplings between doubly occupied MOs and SOMO will lead to largely positive *g*-shift components. The occurrence of both negative and positive *g*-shifts in the present complexes arises from the simultaneous importance of both types of couplings, with similar magnitudes (the negative Δg_{11} arises partly also from higher-order SO contributions, see Discussion above).

The **g**-tensor excitation analysis for the anionic complexes turns out to be much more complicated than for the cations, as double-SOMO and SOMO-virtual excitation contributions are now of even more similar magnitude, whereas the "ligand-field" double-SOMO contributions dominated still for g_{22} and g_{33} in the cationic complexes. As we saw above (Figure 5), we have to distinguish three different types of tensor orientations in the anions. Starting with the first two ligands (L_{NO}, L_{NS}), the largest g_{33} value roughly along the M−N bond (Figure 5b) arises from a compensation between about +38 to +44 ppt double-SOMO and about −22 to −23 ppt SOMO-virtual excitations. As quite a number of orbitals contribute, the analysis is difficult. This arises probably from the rather delocalized nature of the SOMO (Figure 2), which obviously resembles the LUMO in the cationic complexes (Figure S1). The largest positive contributions to g_{33} come from coupling with the HOMO-1, which is largely a metal d-orbital slightly tilted out of the ligand plane (and resembles the HOMO in the cationic complexes; Figure S1). This explains partly the orientation of g_{33} in these two anions (Figure 5b). The largest negative contributions to all components arise from couplings from the α-SOMO to virtual orbitals with predominantly M-acac *σ*-antibonding character.

The anionic complexes with L_{OO} and L_{SS} ligands exhibit more positive values for all three tensor components than the complexes with L_{NO} or L_{NS}, and a very different tensor orientation (cf. Figure 5), with g_{33} perpendicular to the plane of L and g_{11} along the bisector of the chelate bite angle. With L_{OO}, the orientation of g_{33} arises predominantly from a very effective positive HOMO−SOMO coupling (due to a very small energy denominator). Already for L_{SS}, the situation is more complicated. In general, however, the most notable effect of the *π*-donor character of L is an energy increase (and a notable reorientation; cf. Figure S1 in Supporting Information) of the HOMO, which brings HOMO and SOMO closer together. The SOMO-virtual couplings do not appear to be affected that much.

Finally, the tensor for $[Ru(acac)_2(L_{NN})]^-$ differs strongly from those of all other anions, both in magnitude (cf. negative *g*-shifts in Table 5) and in orientation (Figure 5c and discussion above). This may be rationalized mainly by the fact that, due to the relatively poor *π*-donor character of the diiminoquinone ligand L, the spin density in this system is much more localized on L than for the other anions, with much less spin polarization toward the metal (cf. Table 3 and discussion above). This leads in particular to relatively small positive *g*-shift contributions from double-SOMO couplings to g_{33} and g_{11} (about +4 ppt and about −10 ppt, respectively; the contributions to g_{22} sum to about +35 ppt), whereas the negative SOMO-virtual couplings contribute still appreciably to g_{11} and g_{22} (about −22, −50, −12 ppt for g_{11}, g_{22}, and g_{33}, respectively). The deviating **g**-tensor for this system is thus rooted in a somewhat different character of the bonding between metal and quinonoid ligand. The **g**-tensor for this as yet unknown complex provides an interesting prediction (keeping the underlying inaccuracies of the DFT calculations in mind).

The Origin of Spin Contamination: A Closer Look at the Bonding Situation. Previous computational work in our group has identified spin contamination as a potential problem in DFT calculations of the EPR parameters of transition metal complexes.[32,63] While admixture of Hartree−Fock exchange into hybrid functionals was shown to improve in many cases the agreement with experiment for both hyperfine couplings (due to the improved core−shell spin polarization[63]) and **g**-tensors,[32] the onset of significant spin contamination (as measured by the S^2 expectation value of the KS determinant[62]) with increasing HF exchange tended to deteriorate both properties (including the otherwise not very sensitive dipolar metal hyperfine couplings[63]) for some systems. Closer analysis indicated[74] that spin contamination in typical complexes with predominantly metal-centered spin density arises in particular when the SOMO exhibits appreciable metal−ligand antibonding character. The spin contamination was found to be related to appreciable spin polarization of doubly occupied valence orbitals, mainly of metal−ligand bonding character,[74] coupled to the admixture of low-lying excited states of higher spin multiplicity.

The observed increase of spin contamination with increasing HF exchange[32,63] becomes then understandable, as unrestricted Hartree−Fock wave functions tend to appreciably overestimate spin polarization. A larger fraction of HF exchange will thus make the wave function more unstable with respect to admixture of high-spin contaminants. Therefore, the trends in the $\langle S^2\rangle$ expectation values of several of the cationic complexes in Table 5 were very unexpected (the anionic complexes show very small spin contamination and no unusual trends): While the complexes with sulfur donor atoms in the quinonoid ligand (i.e., with L_{NS} and L_{SS}) exhibit the expected increase of spin contamination along the series BP86 < B3LYP < BHLYP, all other cationic complexes have the largest values for the B3LYP functional, and a lower value for BHLYP. Except for one case (L_{NN}, but note the small difference of only 0.02), the BHLYP $\langle S^2\rangle$ value is even below the BP86 value (Table 5)! To our knowledge, behavior like this has not been observed before, and it is worth a closer analysis.

We recall that the predominantly metal-centered spin density in the cationic complexes arises primarily from spin-polarization contributions (cf. Table 3 and Figure 4). However, this alone does not explain the different dependence of $\langle S^2\rangle$ on HF exchange admixture for, e.g. $[Ru(acac)_2(L_{NO})]^+$ and $[Ru(acac)_2$-

---

(73) For similar phenomena in the context of NMR chemical shifts, see: Auer, D.; Strohmann, C.; Arbuznikov, A. V.; Kaupp, M. *Organometallics* **2003**, *22*, 2442. Ruiz-Morales, Y.; Schreckenbach, G.; Ziegler, T. *Organometallics* **1996**, *15*, 3920.

(74) Munzarová, M. L.; Kubáček,P.; Kaupp, M. *J. Am. Chem. Soc.* **2000**, *112*, 11900.

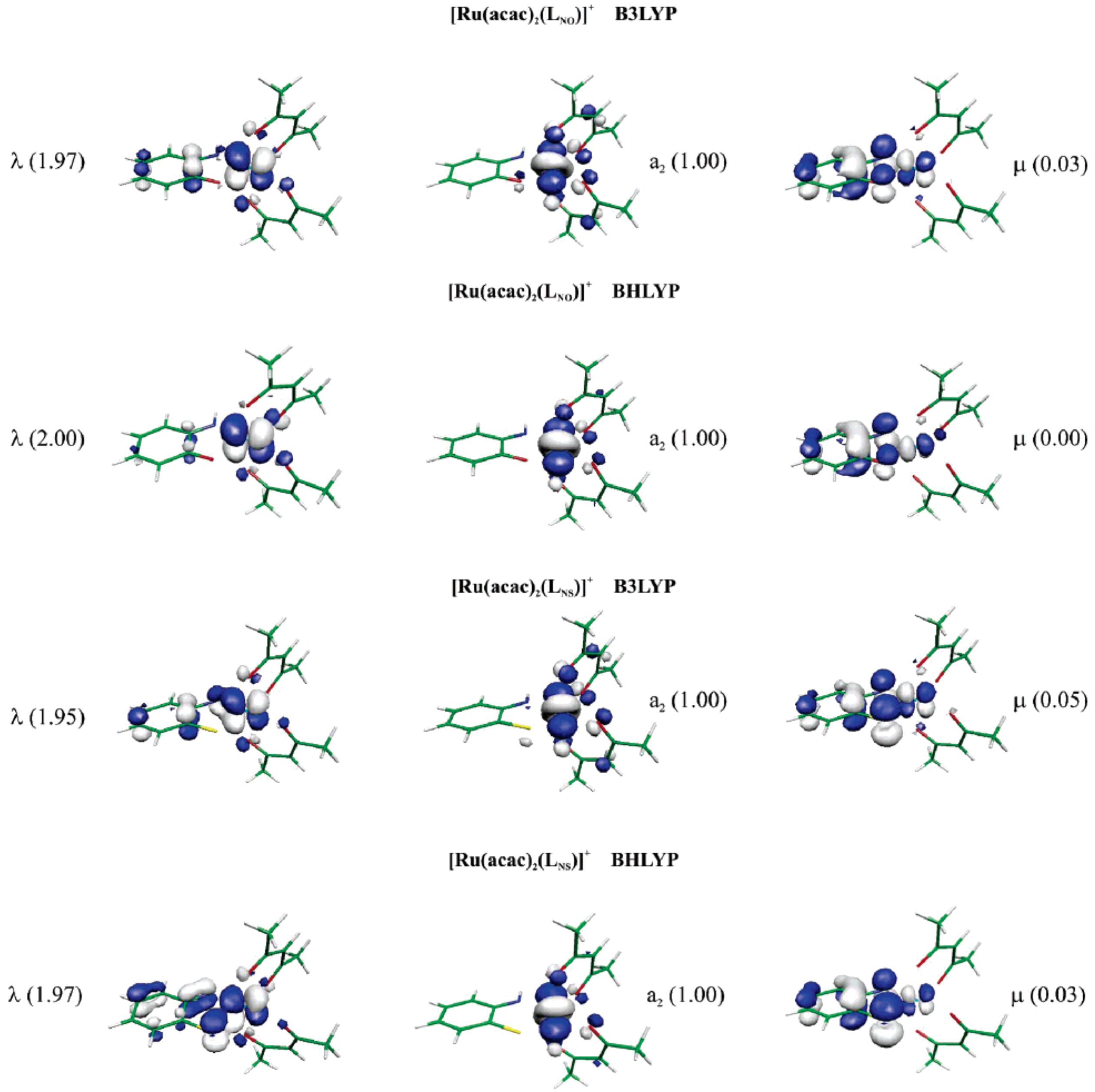
$[Ru(acac)_2(L_{NO})]^+$ B3LYP

$[Ru(acac)_2(L_{NO})]^+$ BHLYP

$[Ru(acac)_2(L_{NS})]^+$ B3LYP

$[Ru(acac)_2(L_{NS})]^+$ BHLYP

Figure 6. Active and singly occupied unrestricted natural orbitals (NOs) for $[Ru(acac)_2(L_{NO})]^+$ and $[Ru(acac)_2(L_{NS})]^+$. B3LYP and BHLYP results are compared. Natural orbital occupancies are given in parentheses. At the given threshold of 0.01 au, no active orbitals are found at BHLYP level for the anionic systems.

$(L_{NS})]^+$. In both cases, the SOMO has appreciable spin density on the acac ligands, which is largely compensated by the negative spin-polarization contributions (Figure 4). Notably, however, for the sulfur-containing complex increasing admixture of HF exchange builds up strong negative spin density, caused by spin polarization, on certain atoms within the quinonoid ligand. In contrast, for $[Ru(acac)_2(L_{NO})]^+$ this negative spin density is already less pronounced at B3LYP level and vanishes essentially with BHLYP. As a result, appreciable negative total spin density remains on N, C2, C4, and C6, in $[Ru(acac)_2(L_{NS})]^+$ but not in $[Ru(acac)_2(L_{NO})]^+$ (Figure 4). Figure S3 in Supporting Information deconstructs the spin-polarization part of the total spin density of $[Ru(acac)_2(L_{NO})]^+$ into the major contributions from individual doubly occupied MOs, both for B3LYP and for BHLYP functionals. Negative spin polarization on oxygen in L arises mainly from the HOMO for B3LYP, and this contribution vanishes for BHLYP.

Obviously, the presence of spin polarization alone does not explain the strange trends of spin contamination for some of the cationic complexes (even the anionic complexes exhibit strong spin polarization; Figure 3, Table 4). The observed differences in the accumulation of negative spin density on some atoms in the quinonoid ligand is, however, at the heart of the different spin contamination. Examination of unrestricted natural orbitals (NOs; Figure 6) allows a deeper rationalization. In the absence of spin contamination one would expect for these complexes only one singly occupied NO together with exactly doubly occupied or exactly empty NOs.[75] Spin contamination

---

(75) See, e.g.: Zilberberg, I.; Ruzankin, S. Ph. *Chem. Phys. Lett.* **2004**, *394*, 165 and references therein.

will appear as a depletion of some formally doubly occupied NOs and concomitant partial occupation of formally empty NOs. Fortunately, in the title systems this pertains only to maximally one pair of a formally occupied and a formally empty NO (termed λ and μ, respectively, in Figure 6). The singly occupied NO is termed a_2. It resembles the canonical SOMO (Figure 2), but with somewhat less delocalization onto the acac ligands.

Most interestingly, the deviation of λ and μ NOs from integer occupation in $[Ru(acac)_2(L_{NO})]^+$ is notable for B3LYP but below the chosen threshold of 0.01 au for BHLYP (Figure 6). In contrast, in $[Ru(acac)_2(L_{NS})]^+$ the NOs deviate from integer occupation for both functionals. Closer inspection indicates notable differences between the character of these NOs for the two complexes. In $[Ru(acac)_2(L_{NO})]^+$, the λ NO is largely nonbonding between the metal and the quinonoid ligand, whereas the μ NO is moderately metal−ligand antibonding (less so for BHLYP than for B3LYP). The presence of sulfur in $[Ru(acac)_2(L_{NS})]^+$ alters the situation. Now the λ-NO is already appreciably Ru−N bonding at B3LYP level and becomes even more strongly Ru−S bonding with BHLYP. The μ-NO is generally more appreciably antibonding than in the absence of sulfur (Figure 6). In agreement with previous analyses,[74] the enhanced spin contamination with increasing HF exchange admixture for $[Ru(acac)_2(L_{NS})]^+$ is thus related to spin polarization across a relatively covalent metal−ligand bond. In contrast, in $[Ru(acac)_2(L_{NO})]^+$ the increased HF exchange admixture leads essentially to a demixing of λ and μ NOs (less interactions between metal and ligand), due to the increased bond ionicity. We conclude thus that the unusual trend in the $\langle S^2\rangle$ values for the cationic complexes without sulfur ligands are due to an interplay between two opposing trends: Increasing HF exchange admixture renders the metal−ligand bond more ionic, and at the same time it increases general spin polarization. While the latter effect tends to increase $\langle S^2\rangle$, the former counteracts this trend by diminishing the involvement of the metal−ligand bond in the spin polarization process. Covalency is more pronounced in the presence of sulfur, and increased spin polarization pervails over a reduction of covalency.

4. Conclusions

The involvement of redox-active ligands is known to be vital to many important biological redox processes catalyzed by metalloenzymes.[3,10,11] However, the determination of the actual redox state of metal and ligand(s) in such systems along redox transformations is often far from trivial (the ligand spin and charge state may sometimes even depend on the protein environment[76]). Here we have shown for a series of ruthenium complexes with biologically relevant *o*-quinone-type ligands, that the formal redox state of metal and ligand may be bracketed in remarkable detail by state-of-the-art quantum chemical tools. Indeed, the careful combination of spin-density, charge-density, and different molecular-orbital analyses, together with studies of molecular structure and electronic **g**-tensors, provided a much more refined view of redox states than previous analyses of experimental structures and EPR spectra alone.

In particular, the singlet closed-shell ground state of the neutral title complexes $[Ru(acac)_2(L)]$ (L = *o*-quinonoid ligand) turns out to be better described by a superposition of Ru^{III}/L^- and Ru^{II}/L^0 states rather than by a pure Ru^{III}/L^- formulation. The anionic complexes are best described as intermediate between Ru^{III}/L^{2-} and Ru^{II}/L^-. In contrast, the triplet excited state of the neutral complexes comes close to a pure Ru^{III}/L^- description, and the cationic complexes appear best described by an assignment Ru^{III}/L^0. In view of the computed structure parameters for various systems, these findings require some modification of previously proposed interrelations between intraligand bond lengths and possible integer “physical” redox states of metal and ligand.[58] Often, the true situation in a given complex may be intermediate between integer oxidation numbers, and the structural data are expected to reflect this.

A somewhat surprising finding of this study is the appreciable importance of spin polarization in the unrestricted Kohn−Sham description of electronic structure and formal redox states for the open-shell systems. This holds both for the anionic and for the cationic complexes, as well as for the triplet excited state of the neutral complexes. While the metal−ligand antibonding SOMOs were delocalized to an unrealistically large extent onto the ligands (mainly onto L for the anions and onto acac for the cations), spin polarization of doubly occupied MOs with more or less metal−ligand bonding character remedied the situation and provided a rather different final charge- and spin-density distribution (with the interesting exception of the as yet unknown anionic complex $[Ru(acac)_2(L_{NN})]^-$). It is likely that this will be a common situation also for DFT calculations on other open-shell transition metal complexes with redox-active ligands. While spin polarization is well-known to be important for the interpretation of electronic structure and spin coupling in multinuclear complexes,[77] we are not aware of any previous study that demonstrated a fundamental importance of spin polarization for the assignment of oxidation state in a mononuclear complex.

We noticed also an unusual behavior of the spin contamination of the Kohn−Sham determinant as a function of exchange-correlation functional for some, but not for all, of the cationic complexes. Closer analysis, in particular of unrestricted natural orbitals, revealed partly counteracting influences from spin polarization and metal−ligand covalency.

The relation of electronic **g**-tensors to electronic structure and spin-density distribution in these nontrivial systems was analyzed by means of MO and atomic spin−orbit analyses in second-order perturbation theory. Starting from a ligand-field theory point of view for the formally low-spin d^5-type cationic complexes, we found that a more refined analysis that includes also SOMO-virtual excitations is necessary to understand in particular the orientation of the g_{33} and g_{22} tensor components. The very different and still more complicated situation for the anionic complexes arises from a similar magnitude of contributions from SOMO to virtual space and from doubly occupied space to SOMO. The orientation of the **g**-tensor in these anionic systems may already be altered fundamentally by a small modification of the quinonoid ligand. Beyond some basic features discussed in the Introduction and except for simple, clear-cut cases, it appears difficult at present to unambiguously assign oxidation states for open-shell complexes with redox-

---

[76] For a relevant recent computational study of heme enzymes, see: de Visser, S. P.; Shaik, S.; Sharma, P. K.; Kumar, D.; Thiel, W. *J. Am. Chem. Soc.* **2003**, *125*, 15779.

[77] See, e.g.: Lovell, T.; Torres, R. A.; Han, W.-G.; Liu, T.; Case, D. A.; Noodleman, L. *Inorg. Chem.* **2002**, *41*, 5744. Stranger, R.; Petrie, S. *J. Chem. Soc., Dalton Trans.* **2002**, 3630. Noodleman, L.; Lovell, T.; Liu, T.; Himo, F.; Torres, R. A. *Curr. Opin. Chem. Biol.* **2002**, *6*, 259.

active ligands based on the **g**-tensors alone. Further quantum chemical analyses, such as the ones presented in this work, appear to be necessary to reach a new level of classification.

Acknowledgment. We are grateful to W. Kaim, B. Sarkar (Stuttgart), and I. Zilberberg (Novosibirsk) for fruitful discussions, and to R. Reviakine, A. Arbouznikov, and A. Patrakov (Würzburg) for technical assistance. This work has been supported by Deutsche Forschungsgemeinschaft (Schwerpunktprogramm “Hochfeld-EPR”, SPP1051, project KA1187/4), and by the graduate college “Moderne Methoden der Magnetischen Resonanz” at Universität Stuttgart. C.R. thanks “Studienstiftung des Deutschen Volkes” for a scholarship.

Supporting Information Available: Tables S1−S5 with Cartesian coordinates of the optimized structures at various computational levels (including **g**-tensor orientations), additional spin-density and NPA analyses, and a breakdown of the $\Delta \mathbf{g}^{SO/OZ}$ contribution of the *g*-shift tensor into metal and ligand contributions; Figures S1−S3 showing the relevant MOs for the calculated complexes, the dependence of spin-density distribution and spin polarization on functional for $[Ru(acac)_2(L_{NN})]^-$, and the analysis of MO spin-polarization contributions to spin density in $[Ru(acac)_2(L_{NO})]^+$. This material is available free of charge via the Internet at http://pubs.acs.org.

JA051811B